A&A 520, A5 (2010)
DOI: 10.1051/0004-6361/200912849

Astronomy & Astrophysics
Special feature

Pre-launch status of the Planck mission

Planck pre-launch status: Low Frequency Instrument calibration and expected scientific performance

A. Mennella[1], M. Bersanelli[1], R. C. Butler[2], F. Cuttaia[2], O. D'Arcangelo[3], R. J. Davis[4], M. Frailis[5], S. Galeotta[5], A. Gregorio[6], C. R. Lawrence[7], R. Leonardi[8], S. R. Lowe[4], N. Mandolesi[2], M. Maris[5], P. Meinhold[8], L. Mendes[9], G. Morgante[2], M. Sandri[2], L. Stringhetti[2], L. Terenzi[2], M. Tomasi[1], L. Valenziano[2], F. Villa[2], A. Zacchei[5], A. Zonca[10], M. Balasini[11], C. Franceschet[1], P. Battaglia[11], P. M. Lapolla[11], P. Leutenegger[11], M. Miccolis[11], L. Pagan[11], R. Silvestri[11], B. Aja[12], E. Artal[12], G. Baldan[11], P. Bastia[11], T. Bernardino[13], L. Boschini[11], G. Cafagna[11], B. Cappellini[10], F. Cavaliere[1], F. Colombo[11], L. de La Fuente[12], J. Edgeley[4], M. C. Falvella[14], F. Ferrari[11], S. Fogliani[5], E. Franceschi[2], T. Gaier[7], F. Gomez[15], J. M. Herreros[15], S. Hildebrandt[15], R. Hoyland[15], N. Hughes[16], P. Jukkala[16], D. Kettle[4], M. Laaninen[17], D. Lawson[4], P. Leahy[4], S. Levin[15], P. B. Lilje[18], D. Maino[1], M. Malaspina[2], P. Manzato[5], J. Marti-Canales[19], E. Martinez-Gonzalez[13], A. Mediavilla[12], F. Pasian[5], J. P. Pascual[12], M. Pecora[11], L. Peres-Cuevas[20], P. Platania[3], M. Pospieszalsky[21], T. Poutanen[22,23,24], R. Rebolo[16], N. Roddis[4], M. Salmon[13], M. Seiffert[7], A. Simonetto[3], C. Sozzi[3], J. Tauber[20], J. Tuovinen[25], J. Varis[25], A. Wilkinson[4], and F. Winder[4]

[1] Università degli Studi di Milano, Dipartimento di Fisica, via Celoria 16, 20133 Milano, Italy
e-mail: aniello.mennella@fisica.unimi.it
[2] INAF-IASF – Sezione di Bologna, via Gobetti 101, 40129 Bologna, Italy
[3] CNR – Istituto di Fisica del Plasma, via Cozzi 53, 20125 Milano, Italy
[4] Jodrell Bank Centre for Astrophysics, School of Physics & Astronomy, University of Manchester, Manchester, M13 9PL, UK
[5] INAf – Osservatorio Astronomico di Trieste, via Tiepolo 11, 34143 Trieste, Italy
[6] Università degli Studi di Trieste, Dipartimento di Fisica, via Valerio 2, 34127 Trieste, Italy
[7] Jet Propulsion Laboratory, California Institute of Technology, 4800 Oak Grove Drive, Pasadena, CA 91109, USA
[8] University of California at Santa Barbara, Physics Department, Santa Barbara CA 93106-9530, USA
[9] *Planck* Science Office, European Space Agency, ESAC, PO box 78, 28691 Villanueva de la Caada, Madrid, Spain
[10] INAF-IASF – Sezione di Milano, via Bassini 15, 20133 Milano, Italy
[11] Thales Alenia Space Italia, S.S Padana Superiore 290, 20090 Vimodrone (Milano), Italy
[12] Departamento de Ingeniera de Comunicaciones, Universidad de Cantabria, Avenida De Los Castros, 39005 Santander, Spain
[13] Instituto de Fisica De Cantabria, Consejo Superior de Investigaciones Cientificas, Universidad de Cantabria, Avenida De Los Castros, 39005 Santander, Spain
[14] Agenzia Spaziale Italiana, Viale Liegi 26, 00198 Roma, Italy
[15] Instituto de Astrofisica de Canarias, vía Láctea, 38200 La Laguna (Tenerife), Spain
[16] DA-Design Oy, Keskuskatu 29, 31600 Jokioinen, Finland
[17] Ylinen Electronics Oy, Teollisuustie 9 A, 02700 Kauniainen, Finland
[18] Institute of Theoretical Astrophysics, University of Oslo, PO box 1029 Blindern, 0315 Oslo, Norway
[19] Joint ALMA Observatory, Las Condes, Santiago, Chile
[20] Research and Scientific Support Dpt, European Space Agency, ESTEC, Noordwijk, The Netherlands
[21] National Radio Astronomy Observatory, 520 Edgemont Road, Charlottesville VA 22903-2475, USA
[22] University of Helsinki, Department of Physics, PO Box 64 (Gustaf Hllstrmin katu 2a), 00014 Helsinki, Finland
[23] Helsinki Institute of Physics, PO Box 64 (Gustaf Hllstrmin katu 2a), 00014 Helsinki, Finland
[24] Metsähovi Radio Observatory, Helsinki University of Technology, Metshovintie 114 02540 Kylmälä, Finland
[25] MilliLab, VTT Technical Research Centre of Finland, Tietotie 3, Otaniemi, Espoo, Finland

Received 8 July 2009 / Accepted 12 January 2010

ABSTRACT

We present the calibration and scientific performance parameters of the *Planck* Low Frequency Instrument (LFI) measured during the ground cryogenic test campaign. These parameters characterise the instrument response and constitute our optimal pre-launch knowledge of the LFI scientific performance. The LFI shows excellent $1/f$ stability and rejection of instrumental systematic effects; its measured noise performance shows that LFI is the most sensitive instrument of its kind. The calibration parameters will be updated during flight operations until the end of the mission.

Key words. cosmic microwave background – telescopes – space vehicles: instruments – instrumentation: detectors – instrumentation: polarimeters – submillimeter: general

1. Introduction

The Low Frequency Instrument (LFI) is an array of 22 coherent differential receivers at 30, 44, and 70 GHz onboard the European Space Agency *Planck*[1] satellite. In 15 months[2] of continuous measurements from the Lagrangian point L_2, *Planck* will provide cosmic-variance- and foreground-limited measurements of the cosmic microwave background temperature anisotropies by scanning the sky in almost great circles with a 1.5 m dual reflector aplanatic telescope (Tauber et al. 2010; Martin et al. 2004; Villa et al. 2002; Dupac & Tauber 2005).

The LFI shares the focal plane of the *Planck* telescope with the High Frequency Instrument (HFI), an array of 52 bolometers in the 100–857 GHz range, cooled to 0.1 K. This wide frequency coverage, necessary for optimal component separation, constitutes a unique feature of *Planck* and a formidable technological challenge, because it requires the integration of two different technologies with different cryogenic requirements in the same focal plane.

Excellent noise performance is obtained with receivers based on indium phosphide high electron mobility transistor amplifiers, cryogenically cooled to 20 K by a vibrationless hydrogen sorption cooler, which provides more than 1 W of cooling power at 20 K. The LFI thermal design has been driven by an optimisation of receiver sensitivity and available cooling power; in particular, radio frequency (RF) amplification is divided between a 20 K front-end unit and a ~300 K back-end unit connected by composite waveguides (Bersanelli et al. 2010).

The LFI has been developed following a modular approach in which the various sub-units (e.g., passive components, receiver active components, electronics) have been built and tested individually before proceding to the next integration step. The final integration and testing phases have been the assembly, verification, and calibration of both the individual radiometer chains (Villa et al. 2010) and the integrated instrument.

In this paper, we focus on the calibration, i.e., the set of parameters that provides our most accurate knowledge of the instrument's scientific performance. After an overview of the calibration philosophy, we focus on the main calibration parameters measured during test campaigns performed at instrument and satellite levels. Information concerning the test setup and data analysis methods is provided where necessary, with references to appropriate technical articles for further details. The companion article that describes the LFI instrument (Bersanelli et al. 2010) is the most central reference for this paper.

The naming convention that we use for receivers and individual channels is given in Appendix A.

2. Overview of the LFI pseudo-correlation architecture

We briefly summarise the LFI pseudo-correlation architecture. Further details and a more complete treatment of the instrument can be found in Bersanelli et al. (2010).

In the LFI, each receiver couples with the *Planck* telescope secondary mirror by means of a corrugated feed horn feeding an orthomode transducer (OMT) that divides the incoming wave into two perpendicularly polarised components, which propagate through two independent pseudo-correlation receivers with HEMT (high electron mobility transistor) amplifiers divided into a cold (~20 K) and a warm (~300 K) stage connected by composite waveguides.

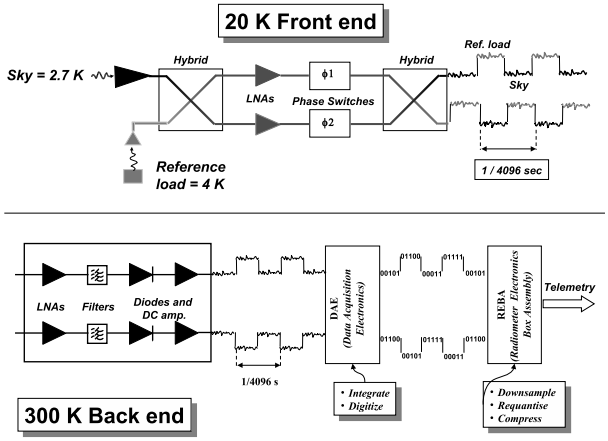

Fig. 1. Schematic of the LFI pseudo-correlation architecture.

A schematic of the LFI pseudo-correlation receiver is shown in Fig. 1. In each radiometer connected to an OMT arm, the sky signal and the signal from a stable reference load thermally connected to the HFI 4 K shield (Valenziano et al. 2009) are coupled to cryogenic low-noise HEMT amplifiers by means of a 180° hybrid. One of the two signals runs through a switch that applies a phase shift, which oscillates between 0 and 180° at a frequency of 4096 Hz. A second phase switch is present in the second radiometer leg to ensure symmetry, but it does not introduce any phase shift. The signals are then recombined by a second 180° hybrid coupler, producing a sequence of sky-load outputs alternating at twice the frequency of the phase switch.

In the back-end of each radiometer (see bottom part of Fig. 1), the RF signals are further amplified, filtered by a low-pass filter and then detected. After detection, the sky and reference load signals are integrated and digitised in 14-bit integers by the LFI digital acquisition electronics (DAE) box.

According to the scheme described above, the radiometric differential power output from each diode can be written as

$$p_{\rm out} = aG_{\rm tot}k\beta\left[T_{\rm sky} + T_{\rm noise} - r\,(T_{\rm ref} + T_{\rm noise})\right],$$
$$r = \frac{\langle V_{\rm out}^{\rm sky}\rangle}{\langle V_{\rm out}^{\rm ref}\rangle}, \qquad (1)$$

where the gain modulation factor, r, minimises the effect of the input signal offset between the sky (~2.7 K) and the reference load (~4.5 K). The effect of reducing the offset in software and the way r is estimated from flight data are discussed in detail in Mennella et al. (2003).

3. Calibration philosophy

The LFI calibration plan was designed to ensure optimal measurement of all parameters characterising the instrument response. Calibration activities have been performed at various levels of integration, from single components, to the integrated instrument and the entire satellite. The inherent redundancy of this approach provided maximum knowledge about the instrument and its subunits, as well as calibration at different levels.

[1] *Planck* http://www.esa.int/Planck is a project of the European Space Agency – ESA – with instruments provided by two scientific Consortia funded by ESA member states (in particular the lead countries: France and Italy) with contributions from NASA (USA), and telescope reflectors provided in a collaboration between ESA and a scientific Consortium led and funded by Denmark.

[2] There are enough consumables onboard to allow operation for an additional year.

Table 1 gives the main LFI instrument parameters and the integration levels at which they have been measured. Three main groups of calibration activities are identified: (i) basic calibration (Sect. 5.1); (ii) receiver noise properties (Sect. 5.2); and (iii) susceptibility (Sect. 5.3).

A particular point must be made about the front-end bias tuning, which is not part of calibration but is nevertheless a key step in setting the instrument scientific performance. To satisfy tight mass and power constraints, power bias lines have been divided into four common-grounded power groups, with no bias voltage readouts. Only the total drain current flowing through the front-end amplifiers is measured and is available in the housekeeping telemetry. This design has important implications for front-end bias tuning, which depends critically on the satellite electrical and thermal configuration. Therefore, front-end bias tuning has been repeated at all integration stages, and will also be repeated in-flight before the start of nominal operations. Details about bias tuning performed at the various integration levels can be found in Davis et al. (2009), Varis et al. (2009), Villa et al. (2010), and Cuttaia et al. (2009).

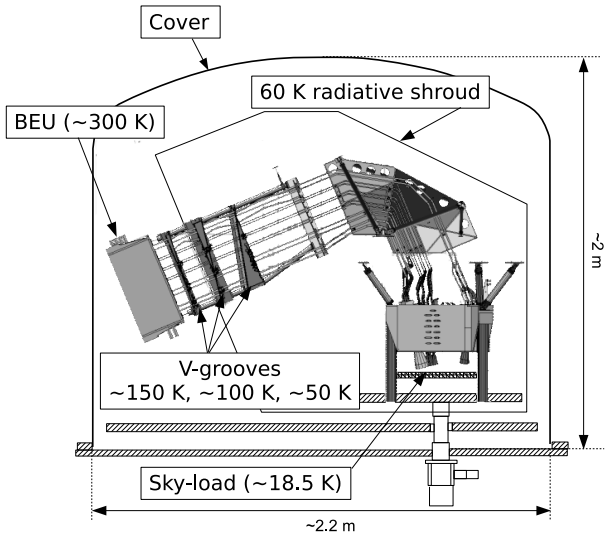

Fig. 2. LFI cryo-chamber facility. The LFI is mounted face-down with the feed horn array facing the eccosorb sky-load.

4. Instrument-level cryogenic environment and test setup

The LFI receivers and the integrated instrument were tested in 2006 at the Thales Alenia Space-Italia laboratories located in Vimodrone (Milano). Custom-designed cryo-facilities were developed to reproduce as closely as possible flight-like thermal, electrical, and data interface conditions (Terenzi et al. 2009a). Table 2 compares the main expected flight thermal conditions with those reproduced during tests on individual receivers and on the integrated instrument.

During the integrated instrument tests, the temperature of the sky and reference loads was much higher than expected in flight (18.5 K vs. 3–4.5 K) as can be seen from the table. To compensate for this, receiver-level tests were conducted with the sky and reference loads at two temperatures, one near flight, the other near 20 K (Villa et al. 2010). During the instrument-level tests, parameters that depend on the sky and reference load temperatures (such as the white noise sensitivity and the photometric calibration constant) could be extrapolated to flight conditions.

4.1. Thermal setup

A schematic of the LFI cryo-facility with the main thermal interfaces is shown in Fig. 2. The LFI was installed face-down, with the feed-horns directed towards an ECCOSORB "sky-load" and the back-end unit resting upon a tilted support. The entire instrument was held in place by a counterweight system that allowed slight movements to compensate for thermal contractions during cooldown. The reference loads were mounted on a mechanical structure reproducing the HFI external interfaces inserted in the middle of the front-end unit.

We summarise here and in Table 3 the main characteristics and issues of the testing environment. Further details about the sky load thermal design can be found in Terenzi et al. (2009a).

Front-end unit. The front-end unit and the LFI main frame were cooled by a large copper flange simulating the sorption cooler cold-end interface. The flange was linked to the 20 K cooler by means of ten large copper braids. Its temperature was controlled by a PID controller, and was stable to ~35 mK at temperatures $\gtrsim$25.5 K at the control stage. The thermal control system was also used in the susceptibility test to change the temperature of the front end in steps (see Sect 5.3).

Sky load. The sky load was thermally linked to the 20 K cooler through a gas heat switch that could be adjusted to obtain the necessary temperature steps during calibration tests. One of the sensors mounted on the central region of the load did not work correctly during the tests and results from the thermal modelling were used to describe its thermal behaviour.

Reference loads. These were installed on an aluminium structure thermally anchored to the 20 K cooler by means of high conductivity straps. An upper plate held all 70 GHz loads, while the 30 and 44 GHz loads were attached to three individual flanges. Two thermometers on the bottom flange were used to measure and control the temperature of the entire structure. Five other sensors monitored the temperatures of the aluminum cases of the reference loads. The average temperature of the loads was around 22.1 K, with typical peak-to-peak stability of 80 mK.

Radiative shroud. The LFI was enclosed in a thermal shield intercepting parasitics and providing a cold radiative environment. The outer surface was highly reflective, while the inner surface was coated black to maximise radiative coupling. Two 50 K refrigerators cooled the thermal shield to temperatures in the range 43–70 K, depending on the distance to the cryocooler cold head, as measured by twelve diode sensors.

Back-end unit. The warm back-end unit was connected to a water circuit with temperature stabilised by a proportional-integral-derivative (PID) controller; this stage was affected by diurnal temperature instabilities of the order of ~0.5 K peak-to-peak. The effect of these temperature instabilities was visible in the total power voltage output from some detectors, but was almost completely removed by differencing.

5. Measured calibration parameters and scientific performance

We present the main calibration and performance parameters (see Table 1).

During the instrument-level test campaign, we experienced two failures: one on the 70 GHz radiometer `LFI18M-0`, and the other on the 44 GHz radiometer `LFI24M-0`. The `LFI18M-0` failure was caused by a phase switch that cracked during cooldown.

Table 1. Main instrument parameters and stages at which they have been measured.

Category	Parameters	Additional Reference	Individual radiometers	Integrated instrument	Satellite	In flight
Bias tuning	Front-end amplifiers	Cuttaia et al. (2009)	Y	Y	Y	Y
	Phase switches	Cuttaia et al. (2009)	Y	Y	Y	Y
		Calibration				
Basic calibration	**Photometric calibration**	Villa et al. (2010)	Y	Y	Y	Y
	Linearity	Mennella et al. (2009)	Y	Y	N	N
	Isolation	Villa et al. (2010)	Y	Y	N	N
	In-band response	Zonca et al. (2009)	Y	N	N	N
Noise performance	**White noise**	Meinhold et al. (2009)	Y	Y	Y	Y
	Knee frequency	Meinhold et al. (2009)	Y	Y	Y	Y
	1/f slope	Meinhold et al. (2009)	Y	Y	Y	Y
Susceptibility	**Front-end temperature fluctuations**	Terenzi et al. (2009b)	Y	Y	Y	Y
	Back-end temperature fluctuations		Y	Y	N	N
	Front-end bias fluctuations		Y	Y	N	N

Notes. In bodface, we highlight calibration parameters defining the instrument scientific performance that are discussed in this paper.

Table 2. Summary of main thermal conditions.

Temperatures	Flight	Receiver	Instr.
Sky	~3 K	≳8 K	≳18.5 K
Ref.	~4.5 K	≳8 K	≳18.5 K
Front-end	~20 K	~20 K	~26 K
Back-end	~300 K	~300 K	~300 K

Notes. The table reports thermal conditions achieved in-flight and in the various testing facilities.

Table 3. LFI cryo-facility thermal performance.

	Avg. Temp. (K)	Stability (K)
Sky load	18–35	0.10
Focal plane unit	26	0.03
Reference loads	22	0.08
Back end unit	315	0.65

Notes. The temperature stability listed in the second column refers to the measured peak-to-peak during one day.

At the end of the test campaign and just before instrument delivery to ESA, the radiometer `LFI18M-0` was replaced with a flight spare. In the second case, the problem was a defective electrical contact to the amplifier V_{g2} (gate 2 voltage) line, which was repaired after the end of the test. Subsequent room-temperature tests as well cryogenic ground satellite tests (Summer 2008) and in-flight calibration (Summer 2009) showed full functionality, confirming the successful repair of `LFI18M-0` and `LFI24M-0`. Because these two radiometers were in a failed state during the test campaign, we generally show no results for them. The only exception is the calibrated noise per frequency channel reported in Table 6, where:

- for `LFI18M-0`, we assume the same noise parameters obtained for `LFI18S-1`; and
- for `LFI24M-0`, we use the noise parameters measured during single-receiver tests before integration into the instrument array.

5.1. Basic calibration

5.1.1. Experimental setup

These parameters were determined by means of tests in which the radiometric average voltage output, V_{out}, was recorded for various input antenna temperature levels, T_{in}. Although straightforward in principle, these tests required the following conditions in the experimental setup and in the measurement

Table 4. Main temperatures during basic calibration.

Step #	T_{sky}(K)	T_{ref} (K)	T_{FEU} (K)	T_{BEU} (C)
1	22.05	22.34	26.40	37.53
2	28.96	22.20	26.45	37.48
3	32.91	22.32	26.40	37.67

procedure to maximise the achieved accuracy in the recovered parameters:

- the sky load temperature distribution had to be accurately known;
- temperature steps had to be sufficiently large (at least a few Kelvin) to dominate over variations caused by $1/f$ noise or other instabilities;
- the reference load temperature had to remain stable during the change in the sky load temperature or, alternatively, variations had to be taken into account in the data analysis, especially in the determination of receiver isolation;
- data points must be acquired at multiple input temperatures to increase the accuracy of the estimates of response linearity.

These conditions were all met during receiver-level tests in which several steps were obtained over a temperature span ranging from ∼8 K to ∼30 K and where the sky-load temperature distrubution was very well known both experimentally and from thermal modelling (Villa et al. 2010).

On the other hand, these conditions were not as well-met during instrument-level tests:

- the total number of available temperature controllers allowed us to place only three sensors on the sky load, one on the back metal-plate, one on the side, and one on the tip of the central pyramid. The input temperature was then determined using the measurements from these three sensors in a dedicated thermal model of the sky load itself;
- the minimum and maximum temperatures that could be set without impacting the focal plane and reference load temperatures were 17.5 K and 30 K, half the range obtained during receiver-level tests;
- the time needed to change the sky load temperature by a few Kelvin was large, of the order of several hours, because of its high thermal mass. This limited to three the number of temperature steps that could be performed in the available time.

The reduced temperature range and number of discrete temperatures that could be set precluded determination of the linearity factor, which was therefore excluded from the fit and constrained to be ±1% about the value found during calibration of individual receivers (see Sect. 5.1.2)[3].

Table 4 summarises temperatures for the three temperature steps considered in these tests. The sky load temperature (antenna temperature) has been determined from the sky load thermal model using temperature sensor data. The reference load temperature is a direct measurement converted into antenna temperature. Front-end and back-end unit temperatures are direct temperature sensor measurements averaged over all sensors.

[3] The slight compression found in the output of the 30 and 44 GHz receivers is caused by the back-end amplifier and diode, which operated in the same conditions during both test campaigns.

5.1.2. Photometric calibration, noise temperature, and linearity

Noise temperatures and calibration constants can be calculated by fitting the $V_{out}(T_{sky})$ data with the most representative model (Daywitt 1989; Mennella et al. 2009)

$$V_{out} = \frac{G_0(T_{sky} + T_{noise})}{1 + b\, G_0(T_{sky} + T_{noise})}, \quad (2)$$

where V_{out} is the voltage output, T_{sky} is the sky load input antenna temperature, T_{noise} is the noise temperature, G_0 is the photometric calibration constant in the limit of linear response, and b is the nonlinearity parameter. For perfectly linear receivers, $b = 0$.

In Table 8, we summarise the best-fit parameters obtained for all the LFI detectors. The nonlinearity parameter b for the 70 GHz receivers is $\lesssim 10^{-3}$, consistent with zero within the measurement uncertainty. The 30 and 44 GHz receivers show some compression at high input temperatures. This nonlinearity arises from the back-end RF amplification stage and detector diode, which show compression down to very low input powers. The nonlinear response has been thoroughly tested both on the individual back end modules (Mennella et al. 2009) and during the RCA calibration campaign (Villa et al. 2010) and has been shown to closely reproduce Eq. (2).

5.1.3. Isolation

Isolation was estimated from the average radiometer voltage outputs, V_{sky} and V_{ref}, at the two extreme sky load temperatures (Steps 1 and 3 in Table 4)[4]. Equations used to calculate isolation values and uncertainties are reported in Appendix B.

In Fig. 3, we summarise the measured isolation for all detectors and provide a comparison with similar measurements performed on individual receiver chains. The results show large uncertainties in isolation measured during instrument-level tests, caused by $1/f$ noise instabilities in the total power datastreams that were not negligible in the time span between the various temperature steps, which was of the order of a few days.

Apart from the limitations given by the measurement setup, the results show that isolation lies in the range −10 dB to −20 dB, which is globally within the requirement of −13 dB.

5.2. Noise properties

The pseudo-correlation design of the *Planck*-LFI receivers has been optimised to minimise the effects of $1/f$ gain variations in the radiometers.

The white noise sensitivity of the receivers is essentially independent of the reference load temperature level (Seiffert et al. 2002) and can be written, in its most general form, as

$$\Delta T_{rms} = K \frac{T_{sky} + T_{noise}}{\sqrt{\beta}}, \quad (3)$$

where β is the receiver bandwidth, ΔT_{rms} is the white noise sensitivity per unit integration time, and K is a constant.

For data obtained from a single diode output, $K = 1$ for unswitched data and $K = 2$ for differenced data. The factor of 2 for differenced data is the product of one $\sqrt{2}$ from the difference

[4] The test can be conducted, in principle, also by changing the reference load temperature. In the instrument cryofacility, however, this was not possible because only the sky load temperature could be controlled.

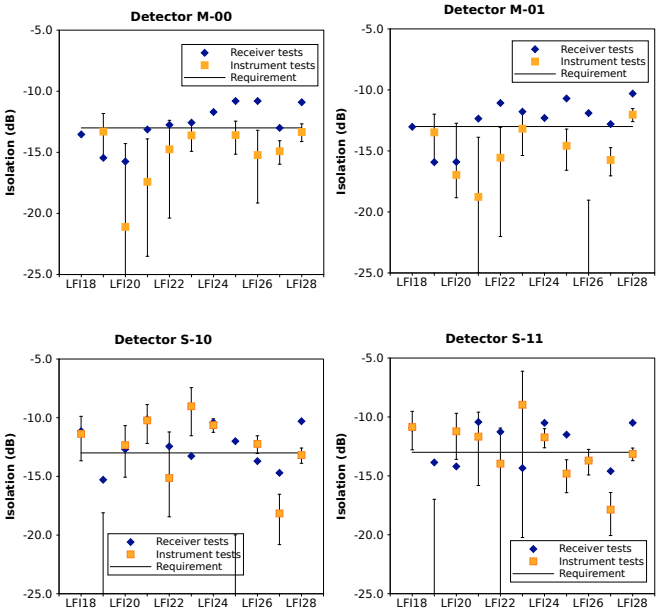

Fig. 3. Summary of measured isolation compared with the same measurements performed at receiver level (Villa et al. 2010).

and another $\sqrt{2}$ from the halving of the sky integration time. When we average the two (calibrated) outputs of each radiometer, we gain back a factor $\sqrt{2}$, so that the final radiometer sensitivity is given by Eq. (3) with $K = \sqrt{2}$.

Figure 4 shows the effectiveness of the LFI pseudo-correlation design (see Meinhold et al. 2009). After differencing, the $1/f$ knee frequency is reduced by more than three orders of magnitude, and the white noise sensitivity scales almost perfectly with the three values of the constant K. The following terminology is used in the figure:

- *Total power data*: datastreams acquired without operating the phase switch;
- *Modulated data*: datastreams acquired in nominal, switching conditions before taking the difference in Eq. (1);
- *Diode differenced data*: differenced datastreams for each diode;
- *Radiometer differenced data*: datastreams obtained from a weighted average of the two diode differenced datastreams for each radiometer (see Eq. (E.2)).

5.2.1. Overview of main noise parameters

If we consider a typical differenced data noise power spectrum, $P(f)$, we can identify three main characterisics:

1. The white noise plateau, where $P(f) \sim \sigma^2$. The white noise sensitivity is given by σ (in units of K s$^{1/2}$), and the noise effective bandwidth by

$$\beta = \frac{(KV_{\rm DC}/\sigma_{\rm V})^2}{\left[1 + bG_0(T_{\rm sky} + T_{\rm noise})\right]^2}, \quad (4)$$

   where $V_{\rm DC}$ is the voltage DC level, $\sigma_{\rm V}$ the uncalibrated white noise sensitivity and the term in square brackets represents the effect of compressed voltage output (see Appendix C).
2. The $1/f$ noise tail, characterised by a power spectrum $P(f) \sim \sigma^2(f/f_k)^{-\alpha}$ described by two parameters: the knee frequency, f_k, defined as the frequency where the $1/f$ and white noise contribute equally, and the slope α.
3. Spurious frequency spikes. These are a common-mode additive effect caused by interference between scientific and housekeeping data in the analog circuits of the data acquisition electronics box (see Sect. 5.2.5).

5.2.2. Test experimental conditions

The test used to determine instrument noise was a long-duration (2-day) acquisition during which the instrument ran undisturbed in its nominal mode. Target temperatures were set at $T_{\rm sky} = 19$ K and $T_{\rm ref} = 22$ K. The front-end unit was at 26 K, maintained to be stable to ±10 mK.

The most relevant instabilities were a 0.5 K peak-to-peak 24-hour fluctuation in the back-end temperature and a 200 mK drift in the reference load temperature caused by a leakage in the gas gap thermal switch that was refilled during the last part of the acquisition (see Fig. 5).

The effect of the reference load temperature variation was clearly identified in the differential radiometric output (see Fig. 6) and removed from the radiometer data before differencing. The effect of the back-end temperature was removed by correlating the radiometric output with temperature sensor measurements.

5.2.3. White noise sensitivity and noise effective bandwidth

There are four sources of white noise that determines the final sensitivity: (i) the input sky signal; (ii) the RF part of the receiver (active components and resistive losses); (iii) the back-end electronics after the detector diode[5]; and (iv) signal quantisation performed in the digital processing unit.

Signal quantisation can significantly increase the noise level if $\sigma/q \lesssim 1$, where q represents the quantisation step and σ the noise level before quantisation. Previous optimisation studies (Maris et al. 2004) demonstrated that a quantisation ratio $\sigma/q \sim 2$ is enough to satisfy telemetry requirements without significantly increasing the noise level. This has been verified during calibration tests using the so-called "calibration channel", i.e., a data channel containing about 15 minutes per day of unquantised data from each detector. The use of the calibration channel allowed a comparison between the white noise level before and after quantisation and compression for each detector. Table 9 summarises these results and shows that digital quantisation caused an increase in the signal white noise of less than 1%.

We report in Fig. 7 the white noise effective bandwidth calculated according to Eq. (4) . Our results indicate that the noise effective bandwidth is smaller than the requirement by 20%, 50%, and 10% at 30, 44, and 70 GHz, respectively. Non-idealities in the in-band response (ripples) causing bandwidth narrowing are discussed in Zonca et al. (2009).

It is useful to extrapolate these results to the expected in-flight sensitivity of the instrument at the nominal temperature of 20 K when observing a sky signal of ∼2.73 K in thermodynamic temperature. This estimate has been performed in two different ways. The first uses measured noise effective bandwidths and noise temperatures in the radiometer equation, Eq. (3). The second starts from measured uncalibrated noise, which is then calibrated in temperature units, corrected for the different focal plane temperature in test conditions, and extrapolated to ∼2.73 K

[5] The additional noise introduced by the analog electronics is generally negligible compared to the intrisic noise of the receiver, and its impact was further mitigated by the variable gain stage after the diode.

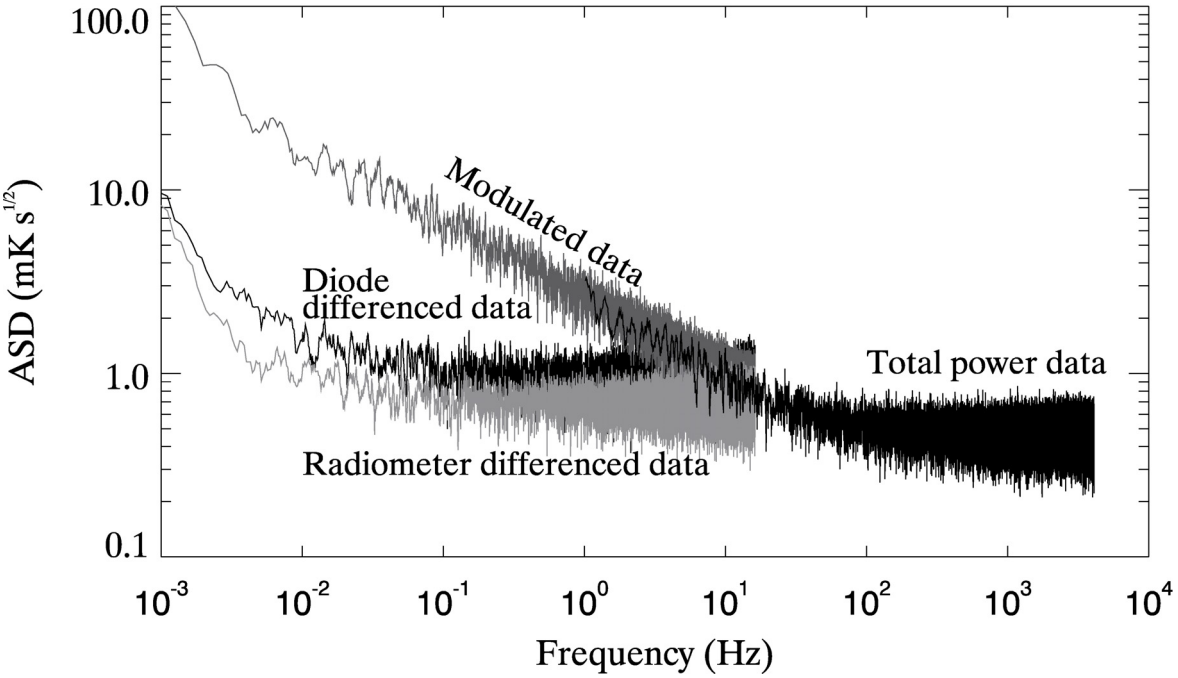

Fig. 4. Amplitude spectral densities of unswitched and differenced data streams. The pseudo-correlation differential design reduces the $1/f$ knee frequency by three orders of magnitude. The white noise level scales almost perfectly with K.

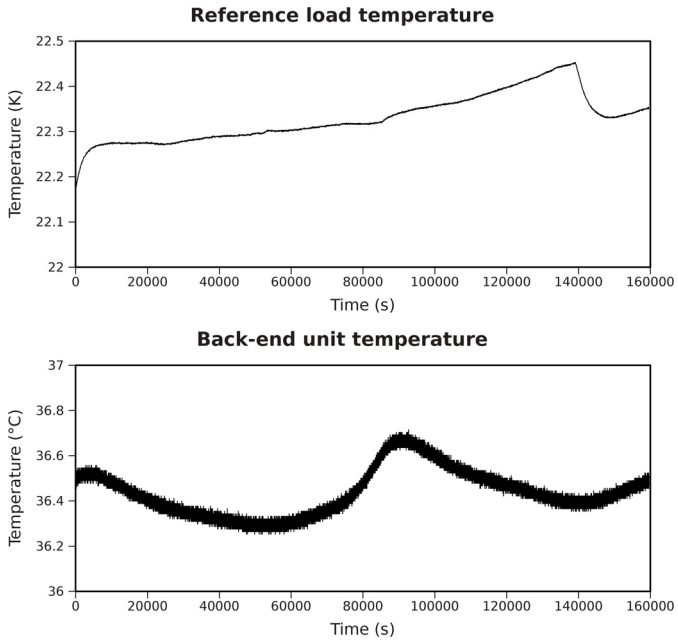

Fig. 5. Thermal instabilities during the long duration acquisition. *Top*: drift in the reference load temperature caused by leakage in the gas cap thermal switch. The drop towards the end of the test coincides with refill of the thermal switch. *Bottom:* 24-h back-end temperature fluctuation.

input using the radiometeric response equation, Eq. (2). The details of the extrapolation are given in Appendix D.

Table 5 indicates the sensitivity per radiometer estimated according to the two procedures. The sensitivity per radiometer was obtained using a weighted noise average from the two detectors of each radiometer (see Appendix E). Because radiometers `LFI18M-0` and `LFI24M-0` were not working during the tests, we estimated the sensitivity per frequency channel by considering the white noise sensitivity of `LFI24M-0`, which was later repaired, measured during receiver-level tests, while for `LFI18M-0`, which was later replaced by a spare unit, we assumed the same sensitivity as for `LFI18S-1`. Further details about the white noise sensitivity of individual detectors are reported in Meinhold et al. (2009).

Table 5. White noise sensitivities per radiometer in $\mu K \cdot s^{1/2}$.

From uncalib. noise	M-0	S-1	From radiom. equation	M-0	S-1
70 GHz			**70 GHz**		
LFI18	468	468	LFI18	450	450
LFI19	546	522	LFI19	482	466
LFI20	574	593	LFI20	498	511
LFI21	424	530	LFI21	381	496
LFI22	454	463	LFI22	428	410
LFI23	502	635	LFI23	453	419
44 GHz			**44 GHz**		
LFI24	372	447	LFI24	404	407
LFI25	501	492	LFI25	451	462
LFI26	398	392	LFI26	455	428
30 GHz			**30 GHz**		
LFI27	241	288	LFI27	311	320
LFI28	315	251	LFI28	305	268

Notes. Sensitivity values have been extrapolated at CMB input using the two methods outlined in the text and detailed in Appendix D.

We provide in Table 6 the sensitivity per frequency channel estimated using the two procedures and compared with the LFI requirement.

5.2.4. 1/f noise parameters

The $1/f$ noise properties of the LFI differenced data were determined more accurately during instrument-level than receiver-level tests for two reasons: (i) the test performed in this phase was the longest of all the test campaign; and (ii) because of the

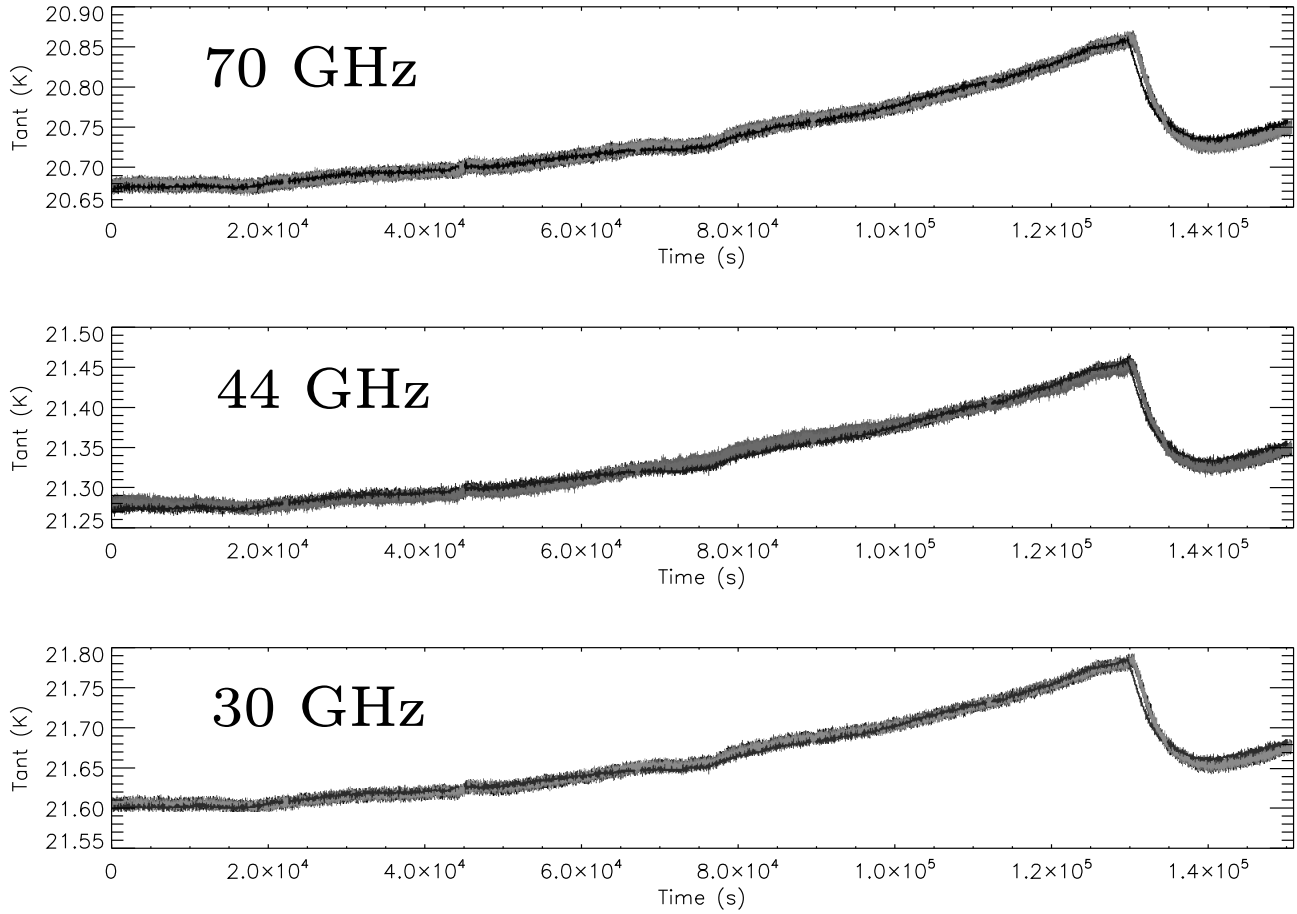

Fig. 6. Calibrated differential radiometric outputs (downsampled to 1 Hz) for all LFI detectors during the long duration test. Temperature sensor data in antenna temperature units are superimposed (thin black line) on the calibrated radiometric data.

Table 6. White noise sensitivities per frequency channel in μK$\cdot$ s$^{1/2}$.

	Meas. noise	Rad. eq.	Req.
70 GHz	146	130	105
44 GHz	174	177	113
30 GHz	135	149	116

Notes. Sensitivity values have been extrapolated at CMB input using the two methods outlined in the text and detailed in Appendix D. The third column reports the LFI requirement.

greater temperature stability, especially compared to the 70 GHz receivers cryofacility (Villa et al. 2010).

Summarised in Table 7, the results show very good $1/f$ noise stability of the LFI receivers, almost all with a knee frequency well below the required 50 mHz.

5.2.5. Spurious frequency spikes

During the FM test campaign, we found unwanted frequency spikes in the radiometeric data at frequencies of the order of a few hertz. The source of the problem was recognised to be in the backend data acquisition electronics box, where unexpected crosstalk between the circuits handling housekeeping and radiometric data affected the radiometer voltage output downstream of the detector diode.

In Fig. 8, this is clearly shown in spectra of unswitched data acquired from the 70 GHz detector `LFI18S-10` with the housekeeping data acquisition activated and deactivated.

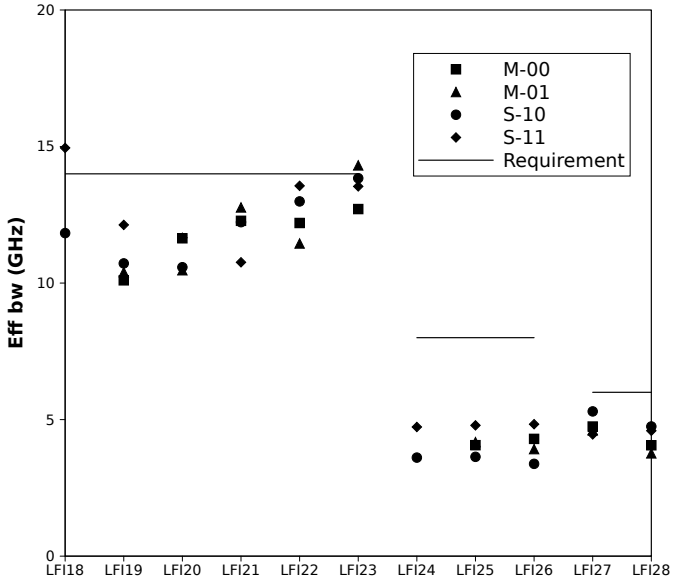

Fig. 7. Noise effective bandwidths calculated during instrument-level measurements. The three lines indicate the 70 GHz, 44 GHz, and 30 GHz requirements.

Because the disturbance is added to receiver signal at the end of the radiometric chain it acts as a common mode effect on both the sky and reference load data so that its effect in differenced data is reduced by several orders of magnitude bringing it well below the radiometer noise level.

Table 7. Summary of knee frequency and slope.

	f_{knee} (mHz)			
	M-00	**M-01**	**S-10**	**S-11**
70 GHz				
LFI18	...	...	61	59
LFI19	25	32	27	37
LFI20	21	19	23	28
LFI21	28	30	41	38
LFI22	46	39	41	76
LFI23	30	31	58	75
44 GHz				
LFI24	...	...	39	46
LFI25	31	31	21	30
LFI26	61	61	61	14
30 GHz				
LFI27	30	30	27	26
LFI28	37	31	37	39

	slope			
	M-00	**M-01**	**S-10**	**S-11**
70 GHz				
LFI18	...	...	−1.12	−1.12
LFI19	−1.27	−1.22	−1.11	−1.02
LFI20	−1.47	−1.64	−1.27	−1.24
LFI21	−1.48	−1.61	−1.15	−1.17
LFI22	−1.18	−1.26	−1.19	−1.01
LFI23	−1.11	−1.19	−1.15	−1.12
44 GHz				
LFI24	...	...	−1.06	−1.11
LFI25	−1.07	−1.03	−1.10	−1.00
LFI26	−1.01	−1.01	−1.05	−1.55
30 GHz				
LFI27	−1.06	−1.13	−1.25	−1.13
LFI28	−0.94	−0.93	−1.07	−1.06

Further analysis of these spikes has shown that the disturbance is synchronized in time. By binning the data synchronously, we obtain a template of the disturbance, which allows its removal in the time-domain (Meinhold et al. 2009). The feasibility of this approach has been proven using data acquired during the full satellite test campaign in Liege, Belgium during July and August, 2008.

Therefore, because the only way to eliminate the disturbance *in hardware* would be to operate the instrument without any housekeeping information, our baseline approach is that, if necessary, the residual effect will be removed from the data in the time domain after measuring the disturbance shape from the flight data.

5.3. Radiometric suceptibility to front-end temperature instabilities

Thermal fluctuations in the receivers result in gain changes in the amplifiers and noise changes in the (slightly emissive) passive components (e.g., horns, OMTs, waveguides). These changes mimic the effect of changes in sky emission, expecially at fluctuation frequencies near the satellite spin frequency. The most important source of temperature fluctuations for LFI is the sorption cooler (Bhandari et al. 2004; Wade et al. 2000).

For small temperature fluctuations in the focal plane, the radiometric response is linear (Seiffert et al. 2002; Terenzi et al. 2009b), so the spurious antenna temperature fluctuation in the differential receiver output can be written as

$$\delta T_{\rm out} = f_{\rm trans} \delta T_{\rm phys}, \tag{5}$$

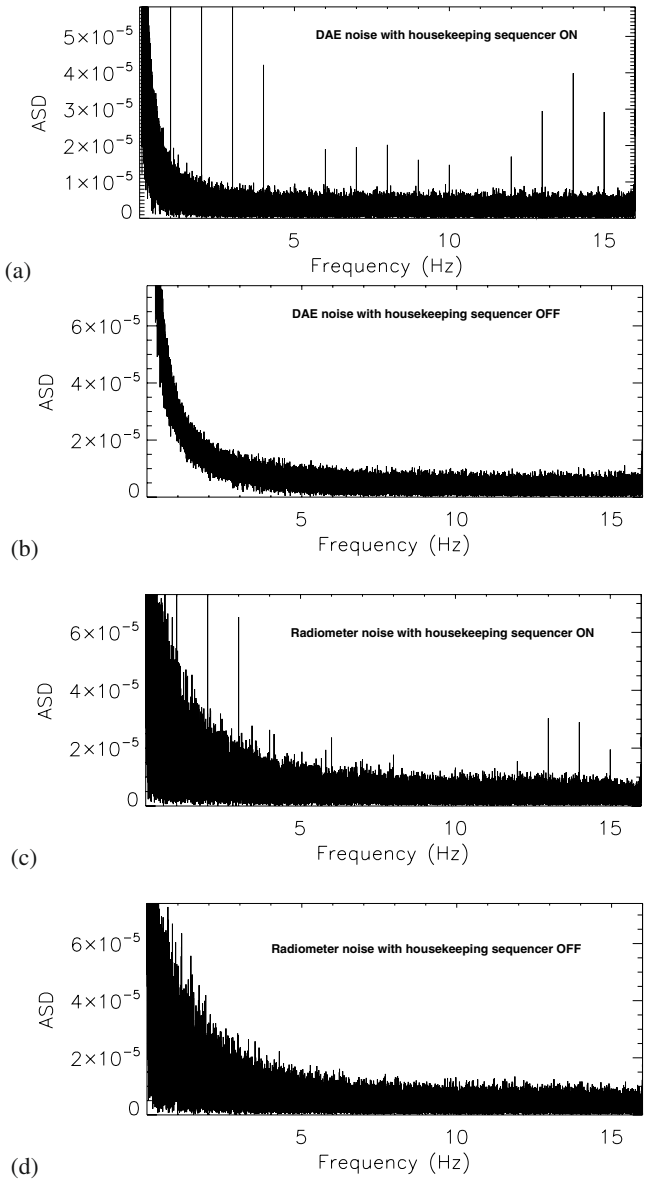

Fig. 8. DAE-only and radiometer noise amplitude density spectra in $V/\sqrt{\rm Hz}$ (from `LFI18S-10` unswitched data) with and without activation of the housekeeping acquisition. These data clearly show that the source of the disturbance is in the data acquisition electronics box and is correlated with the status of the housekeeping data acquisition.

where the transfer function $f_{\rm trans}$ can be estimated analytically from the differential power output given in Eq. (1):

$$f_{\rm trans} = \frac{\partial p_{\rm out}}{\partial T_{\rm phys}} \left(\frac{\partial p_{\rm out}}{\partial T_{\rm sky}} \right)^{-1}. \tag{6}$$

The analytical form of $f_{\rm trans}$ (discussed in detail in Terenzi et al. 2009b) depends primarily on the front-end amplifier susceptibility parameters, $\partial G/\partial T_{\rm phys}$ and $\partial T_{\rm noise}/\partial T_{\rm phys}$, as well as other instrument and boundary condition parameters such as the insertion loss of passive components and the sky input temperature.

If we consider the systematic error budget in Bersanelli et al. (2010), it is possible to derive a requirement for the radiometric transfer function, $f_{\rm trans} \lesssim 0.1$, in order to maintain the final peak-to-peak error per pixel $\lesssim 1$ μK (see Appendix F). During instrument-level calibration activities, dedicated tests were

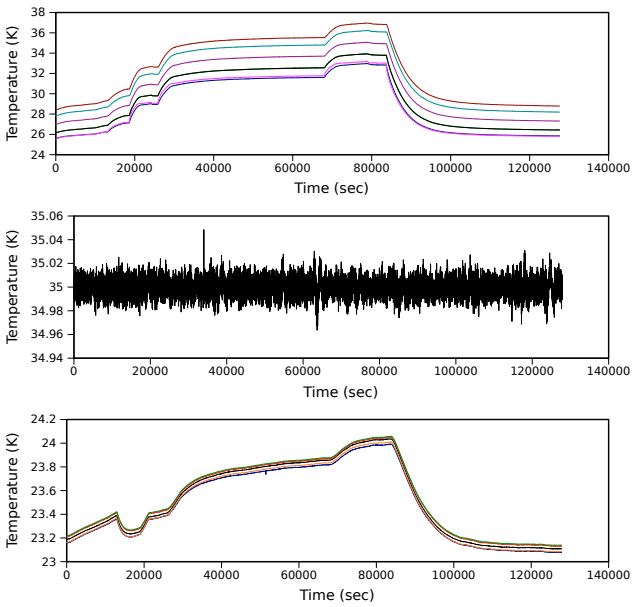

Fig. 9. Behaviour of focal plane (*top*), sky load (*middle*), and reference load (*bottom*) temperatures during the thermal susceptibility tests.

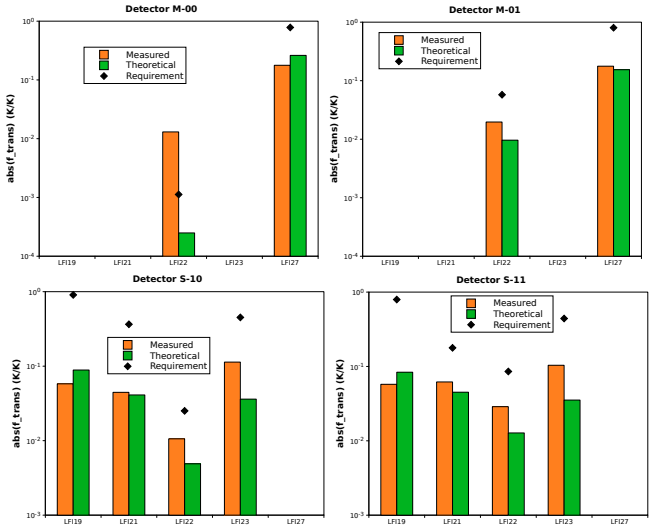

Fig. 10. Measured and predicted radiometric thermal transfer functions, with the scientific requirement rescaled to the experimental conditions of the test. The comparison is possible only for the subset of radiometers that was tuned at the time of this test.

performed to estimate $f_{\rm trans}$ and compare it with theoretical estimates and similar tests performed on individual receivers.

5.3.1. Experimental setup

During this test, the focal plane temperature was varied in steps between between 27 and 34 K. The sky and reference load temperatures were $T_{\rm sky} = 35 \pm 0.01$ K and $T_{\rm ref} = 23.7 \pm 0.5$ K. The reference load temperature showed a non-negligible coupling with the focal plane temperature (as shown in Fig. 9) so that the effect of this variation had to be removed from the data before calculating the thermal transfer function.

Although the test lasted more than 24 h, it was difficult to reach a clean steady state plateau after each step because of the high thermal mass of the instrument. Furthermore, for some detectors the bias tuning was not yet optimised, so that only data from a subset of detectors could be compared with similar measurements performed at receiver-level.

In Fig. 10, we summarise our results by comparing predicted and measured transfer functions for the tested detectors. Predicted transfer functions were calculated using the list of parameters provided in Appendix G, derived from receiver-level tests. In the same figure, we also plot the thermal susceptibility requirement rescaled to the experimental test conditions with a scale factor given by the ratio

$$f_{\rm trans}({\rm ground})/f_{\rm trans}({\rm flight}), \quad (7)$$

where $f_{\rm trans}$ was calculated using Eq. (5) in ground and flight conditions from sky, reference-load, and focal plane temperatures.

Figure 10 shows that transfer functions measured during instrument-level tests are compliant with scientific requirements and reflect theoretical predictions, with the exception of `LFI22` and `LFI23`, which were more susceptible to front-end temperature fluctuations than expected. In general, results from the instrument-level test campaign confirm the design expectations, and suggest that the level of temperature instabilities in the focal plane will not represent a significant source of systematic errors in the final scientific products. This has been further verified during satellite thermal-vacuum tests conducted with the flight model sorption cooler (see Sect. 6.4).

6. Comparison with satellite-level test results

The final cryogenic ground test campaign was conducted at the Centre Spatial de Liège (CSL) with the LFI and the HFI integrated onboard *Planck*. To reproduce flight temperature conditions, the satellite was enclosed in an outer cryochamber cooled to liquid nitrogen temperatures, and surrounded by an inner thermal shield at ~20 K. An ECCOSORB load cooled to 4.5 K was placed between the secondary mirror and the feed horns to simulate the cold sky. For the first time, the LFI focal plane was cooled to 20 K by the sorption cooler, and the reference loads were cooled to ~4 K by the 4 K cooler.

During the CSL tests, we verified instrument functionality, tuned front-end biases and back-end electronics, and assessed scientific performance in the closest conditions to flight attainable on the ground. Front-end bias tuning made use of the ability of the 4 K cooler system to provide several different stable temperatures to the reference loads in the range of 24 K down to the nominal 4 K (Cuttaia et al. 2009).

A detailed description of satellite-level tests is beyond the scope of this paper; here we focus on the comparison of the main performance parameters measured during instrument and satellite tests, and show that despite differences in test conditions the overall behaviour was reproduced.

6.1. White noise sensitivity

Calibrated white noise sensitivities were determined during satellite-level tests by exploiting a ~80 mK variation in the sky load temperature caused by the periodic helium refills of the chamber. This variation allowed us to estimate the photometric calibration constant by correlating the differenced voltage datastream $\delta V(t)$ from each detector with the sky load temperature $T^{\rm ant}_{\rm sky}(t)$ (in antenna temperature units).

To extrapolate the calibrated sensitivity from the 4.5 K input temperature in the test to flight conditions, we calculated the ratio

$$\frac{\Delta T_{\rm rms}(T_{\rm sky}^{\rm flight})}{\Delta T_{\rm rms}(T_{\rm sky}^{\rm CSL})} = \frac{(T_{\rm sky}^{\rm flight} + T_{\rm noise})}{(T_{\rm sky}^{\rm CSL} + T_{\rm noise})}, \quad (8)$$

using the noise temperature found from the non-linear model fit from the receiver-level test campaign (Villa et al. 2010). This ratio ranges from a minimum of ∼0.96 to a maximum of ∼0.98. Exact values for each detector are not reported here for simplicity.

In Fig. 11, we summarise graphically the in-flight sensitivity estimates from the three tests. In the following plots the sensitivity values are provided with errorbars, with the following meanings:

- errorbars in sensitivities estimated from satellite-level data represent the statistical error in the calibration constants calculated from the various temperature jumps and propagated through the sensitivity formulas. They represent genuine statistical uncertainties;
- errorbars in sensitivities estimated from receiver and instrument level tests data represent the uncertainty coming from the calculation performed according to the two different methods described in Sect. 5.2.3 and Appendix D. In this case, errorbars do not have specific statistical significance, but nevertheless provide an indication of the uncertainties in the estimate.

Figure 11 shows that the in-flight sensitivity lies between the requirement and twice the goal levels for the 30 and 70 GHz receivers, and at about twice the goal for the 44 GHz receivers. The agreement between values extrapolated from the three test campaigns is very good, apart from two noticeable outliers, `LFI21S-1` and `LFI24M-0`, which showed a higher noise level during satellite level tests. Investigation showed that this anomaly was caused by incorrect bias voltages on the front-end devices during the test.

After a thorough bias tuning activity conducted during in-flight calibration (see Cuttaia et al. 2009), a new bias configuration was found that normalised the white noise sensitivity of these two receivers, as expected. A full description of the in-flight calibration results and scientific performance will be given in a forthcoming dedicated paper.

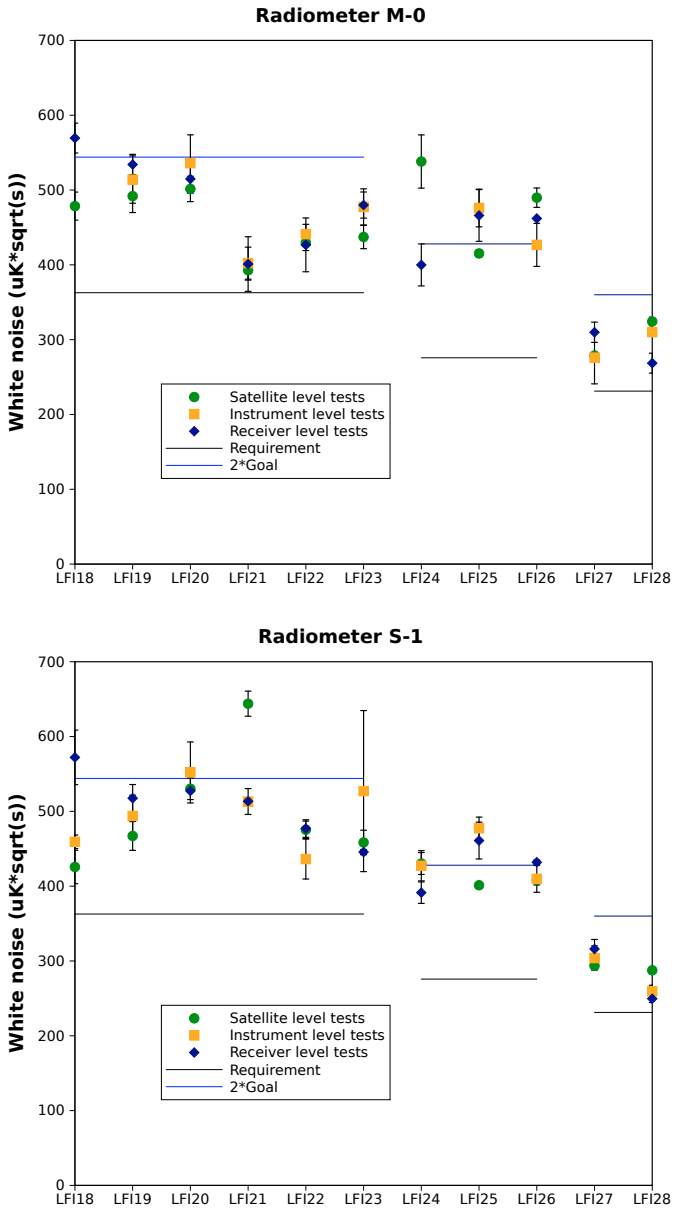

Fig. 11. Summary of in-flight sensitivities per radiometer estimated from receiver, instrument, and satellite-level test campaigns.

6.2. Noise stability

During satellite-level tests, receiver noise stability was determined from stable data acquisitions lasting several hours with the instruments in their tuned and nominal conditions. Figure 12 summarises $1/f$ knee frequencies measured at instrument and satellite levels compared with the 50 mHz requirement, and shows that the noise stability of all channels is within requirements, with the single marginal exception of `LFI23S-11`. The slope ranged from a minimum of 0.8 to a maximum of 1.7.

During satellite-level tests, there was substantial improvement in the noise stability relative to instrument-level tests, in some cases with a reduction in knee frequency of more than a factor of 2. This can be partly explained by the almost perfect signal input balance achieved in the CSL cryo-facility, which was much less than 1 K compared to the ∼3 K obtained in the instrument cryo-facility. Some improvement was also expected because of the much higher thermal stability of the CSL facility. In particular fluctuations of the sky and reference loads in CSL were about two order of magnitudes less than those in the instrument facility (see Table 3). Because the highly balanced input achieved in CSL will not be reproduced in-flight, we expect that the flight knee frequencies will be slightly higher (although similar) than those measured in CSL.

6.3. Isolation

Isolation (see Eq. (B.3)) was measured during the satellite tests by changing the reference load temperature by 3.5 K. Figure 13 compares the isolation measured during receiver- and satellite-level tests. Several channels exceed the −13 dB requirement; a few are marginally below. One channel, `LFI21S-1`, showed poor isolation of only −7 dB. This result is consistent with the high value of the calibrated white noise measured for this channel

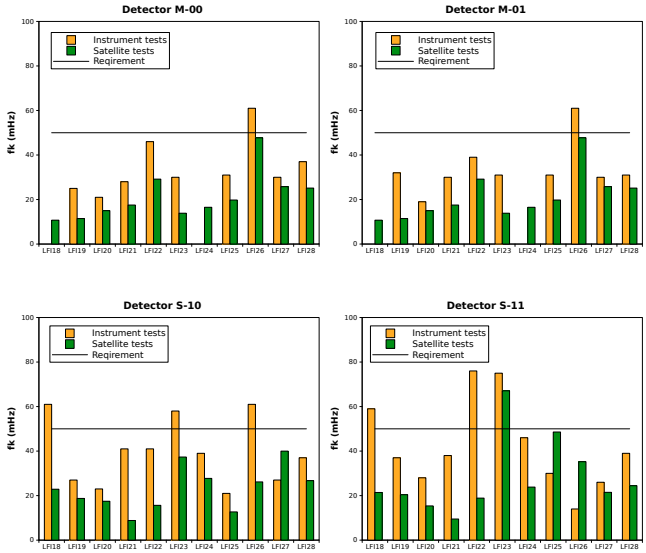

Fig. 12. Summary of $1/f$ knee frequencies measured at instrument and satellite levels.

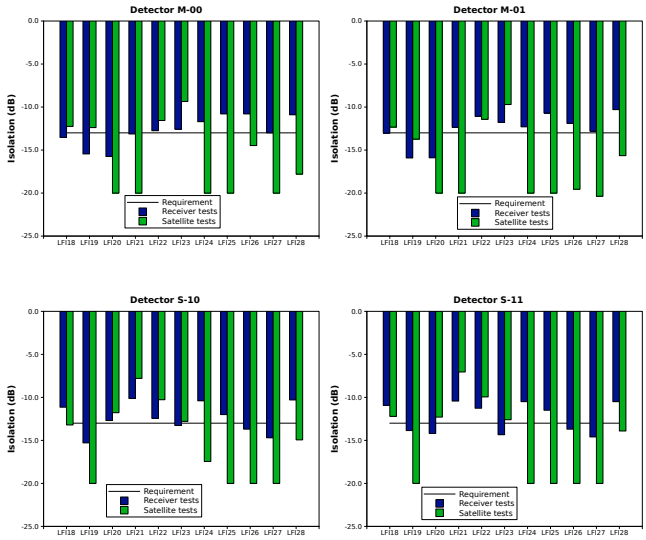

Fig. 13. Summary of isolation measured at receiver and satellite levels.

(see Sect. 6.1), supporting the hypothesis of non-optimal biasing of that channel.

6.4. Thermal susceptibility

As mentioned in Sect. 4.3, the most important source of temperature fluctuations in the LFI focal plane is the sorption cooler. The satellite-level test provided the first opportunity to measure the performance of the full *Planck* thermal system. Fluctuations at the interface between the sorption cooler and the LFI were measured to be about 100 mK peak-to-peak. Using methods described in Mennella et al. (2002), we infer that the effect of these fluctuations will be less than 1 μK per pixel in the maps, in line with the scientific requirements outlined in Bersanelli et al. (2010).

7. Conclusions

The LFI was integrated and tested in thermo-vacuum conditions at the Thales Alenia Space Italia laboratories, located in Vimodrone (Milano), during the summer of 2006. The test goals were a wide characterisation and calibration of the instrument, ranging from functionality to scientific performance assessment.

The LFI was fully functional, apart from two failed components in `LFI18M-0` and `LFI24M-0` that have now been fixed (one replaced and the other repaired) after the cryogenic test campaign, recovering full functionality.

Measured instrument parameters are consistent with measurements performed on individual receivers. In particular, the LFI shows excellent $1/f$ stability and rejection of instrumental systematic effects. Although the very ambitious sensitivity goals have not been fully met, the measured performance makes LFI the most sensitive instrument of its kind, a factor of 2 to 3 superior to WMAP[6] at the same frequencies. In particular at 70 GHz, near the minimum of the foreground emission for both temperature and polarisation anisotropy, the combination of sensitivity and angular resolution of LFI will provide a clean reconstruction

Table 8. Best-fit non-linear model parameters.

Rec. ID	Param.	M-00	M-01	S-10	S-11
	b	...	...	$\lesssim 10^{-3}$	$\lesssim 10^{-3}$
LFI18	G_0 (V/K)	...	...	0.026	0.022
	$T_{\rm noise}$ (K)	...	...	37.4	40.5
	b	$\lesssim 10^{-3}$	$\lesssim 10^{-3}$	$\lesssim 10^{-3}$	$\lesssim 10^{-3}$
LFI19	G_0 (V/K)	0.020	0.021	0.016	0.018
	$T_{\rm noise}$ (K)	39.8	38.7	37.5	40.0
	b	$\lesssim 10^{-3}$	$\lesssim 10^{-3}$	$\lesssim 10^{-3}$	$\lesssim 10^{-3}$
LFI20	G_0 (V/K)	0.019	0.018	0.025	0.025
	$T_{\rm noise}$ (K)	42.3	42.2	43.9	43.0
	b	$\lesssim 10^{-3}$	$\lesssim 10^{-3}$	$\lesssim 10^{-3}$	$\lesssim 10^{-3}$
LFI21	G_0 (V/K)	0.025	0.023	0.016	0.014
	$T_{\rm noise}$ (K)	31.9	34.6	43.3	45.9
	b	$\lesssim 10^{-3}$	$\lesssim 10^{-3}$	$\lesssim 10^{-3}$	$\lesssim 10^{-3}$
LFI22	G_0 (V/K)	0.011	0.012	0.014	0.016
	$T_{\rm noise}$ (K)	40.5	38.9	40.8	43.5
	b	$\lesssim 10^{-3}$	$\lesssim 10^{-3}$	$\lesssim 10^{-3}$	$\lesssim 10^{-3}$
LFI23	G_0 (V/K)	0.025	0.029	0.014	0.007
	$T_{\rm noise}$ (K)	40.6	39.2	50.3	54.2
	b	...	...	1.43	1.43
LFI24	G_0 (V/K)	...	...	0.005	0.005
	$T_{\rm noise}$ (K)	...	...	19.7	19.9
	b	1.21	1.16	0.79	1.00
LFI25	G_0 (V/K)	0.008	0.008	0.007	0.007
	$T_{\rm noise}$ (K)	19.7	19.7	20.5	20.2
	b	1.07	1.40	0.93	1.21
LFI26	G_0 (V/K)	0.005	0.006	0.007	0.007
	$T_{\rm noise}$ (K)	20.2	19.1	18.5	18.1
	b	0.12	0.12	0.12	0.14
LFI27	G_0 (V/K)	0.074	0.081	0.070	0.058
	$T_{\rm noise}$ (K)	13.3	13.1	14.3	13.7
	b	0.19	0.16	0.19	0.19
LFI28	G_0 (V/K)	0.076	0.103	0.071	0.061
	$T_{\rm noise}$ (K)	11.7	11.3	10.9	10.8

Notes. Best-fit parameters have been obtained from the non-linear fit to data acquired during instrument-level tests. The linearity factor was obtained by constraining it to be ±1% around the value found during calibration of individual receivers (see Mennella et al. 2009).

[6] Calculated for the final resolution element per unit integration time.

Table 9. Impact of quantisation and compression on white noise sensitivity.

	M-00			M-01			S-10			S-11		
	σ^1	$\sigma_q{}^2$	Δ^3	σ	σ_q	Δ	σ	σ_q	Δ	σ	σ_q	Δ
70 GHz												
LFI18	...	...	...	...	...	...	38.93	39.22	0.74%	31.07	31.39	1.02%
LFI19	33.50	33.68	0.55%	34.00	34.13	0.39%	25.68	25.85	0.63%	27.48	27.67	0.71%
LFI20	31.08	31.17	0.31%	31.20	31.37	0.54%	44.77	45.14	0.83%	41.95	42.23	0.67%
LFI21	33.77	33.94	0.51%	32.27	32.39	0.35%	26.50	26.67	0.62%	25.63	25.86	0.87%
LFI22	17.03	17.15	0.67%	19.29	19.41	0.61%	20.99	21.05	0.28%	23.94	24.06	0.49%
LFI23	37.84	38.01	0.44%	41.00	41.25	0.61%	23.76	24.01	1.04%	12.15	12.19	0.36%
44 GHz												
LFI24	...	...	...	...	...	...	5.95	5.97	0.25%	5.32	5.35	0.45%
LFI25	7.50	7.54	0.50%	7.53	7.55	0.30%	9.34	9.37	0.35%	6.93	6.96	0.43%
LFI26[4]	6.04	6.06	0.32%	6.18	6.20	0.31%	8.81	8.84	0.28%	...	...	...
30 GHz												
LFI27	62.34	62.67	0.52%	65.62	65.97	0.53%	56.19	56.40	0.37%	52.48	52.59	0.22%
LFI28	52.96	53.27	0.59%	68.34	68.58	0.34%	46.77	46.94	0.35%	44.15	44.24	0.20%

Notes. [1] White noise sensitivity before quantisation and compression in $\mu V/\sqrt{Hz}$. [2] White noise sensitivity after quantisation and compression in $\mu V/\sqrt{Hz}$. [3] Percent relative difference: $\Delta = 100 \times (\sigma_q - \sigma)/\sigma$. [4] No values are given for `LFI26S-11`, for which quantisation and compression parameters were set to incorrect values because of a problem in the software optimisation procedure that was identified and solved after the calibration campaign.

of the temperature power spectrum up to $\ell \sim 1400$ (Mandolesi et al. 2010).

After the instrument test campaign, the LFI was integrated with the HFI and the satellite. Between June and August 2008, *Planck* was tested at the CSL in flight-representative, thermo-vacuum conditions, and showed to be fully functional.

Planck was launched on May 14th from the Guyane Space Centre in Kourou and has reached its observation point, L2. In-flight testing and calibration is underway, and will provide the final instrument tuning and scientific performance assessment. After 17 years, *Planck* is almost ready to begin recording the first light of the Universe.

Acknowledgements. The *Planck*-LFI project is developed by an Interntional Consortium lead by Italy and involving Canada, Finland, Germany, Norway, Spain, Switzerland, UK, USA. The Italian contribution to *Planck* is supported by the Italian Space Agency (ASI). The work in this paper has been supported by in the framework of the ASI-E2 phase of the *Planck* contract. The US *Planck* Project is supported by the NASA Science Mission Directorate. In Finland, the *Planck*-LFI 70 GHz work was supported by the Finnish Funding Agency for Technology and Innovation (Tekes).

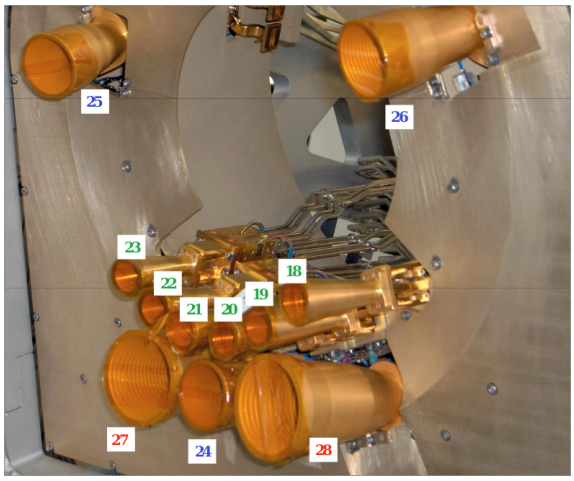

Fig. A.1. Feed horns in the LFI focal plane. Each feed horn is tagged by a label running from LFI18 to LFI28. LFI18 through LFI23 are 70 GHz receivers, LFI24 through LFI26 are 44 GHz receivers, and both LFI27 and LFI28 are 30 GHz receivers.

Appendix A: LFI receiver and channel naming convention

The various receivers are labelled LFI18 to LFI28, as shown in Fig. A.1. The radiometers connected to the two OMT arms are labelled M-0 ("main" OMT arm) and S-1 ("side" OMT arm), while the two output detectors from each radiometer are labelled as 0 and 1. Therefore `LFI18S-10`, for example, refers to detector 0 of the side arm of receiver LFI18, and `LFI24M-01` refers to detector 1 of the main arm of receiver LFI24.

Appendix B: Receiver isolation: definition, scientific requirements, and measurements

B.1. Definition and requirement

In Sect. 2, it is shown that the output of the LFI pseudo-correlation receivers is a sequence of sky and reference load signals alternating at twice the phase switch frequency. If the pseudo-correlator is not ideal, the separation after the second hybrid is not perfect and a certain level of mixing between the two signals will be present in the output. Typical limitations on isolation are (i) imperfect hybrid phase matching; (ii) front-end gain amplitude mismatch; and (iii) mismatch in the insertion loss in the two switch states (Seiffert et al. 2002).

A more general relationship representing the receiver power output can be written as

$$p_{\rm out} = aG_{\rm tot}k\beta\Big[(1-\epsilon)T_{\rm sky} + \epsilon T_{\rm ref} + T_{\rm noise} - r\Big((1-\epsilon)T_{\rm ref} + \epsilon T_{\rm sky} + T_{\rm noise}\Big)\Big], \quad \text{(B.1)}$$

where the parameter ϵ represents the degree of mixing or, in other words, deviation from ideal isolation.

We now consider the receiver scanning the sky and therefore measuring a variation in the sky signal given by the CMB, $\Delta T_{\rm CMB}$. If we define $r = \frac{T_{\rm sky}+T_{\rm noise}}{T_{\rm ref}+T_{\rm noise}}$ and develop Eq. (B.1) in series up to the first order in ϵ, we see that the differential power output is proportional to

$$p_{\rm out} \propto \Delta T_{\rm CMB}\,(1-\delta_{\rm iso})\,, \quad \text{(B.2)}$$

where $\delta_{\rm iso} = \frac{2T_{\rm noise}+T_{\rm sky}+T_{\rm ref}}{T_{\rm noise}+T_{\rm ref}}\epsilon$, which provides a useful relationship for estimating the requirement on the isolation, $\epsilon_{\rm max}$ given an acceptable level of $\delta_{\rm iso}^{\rm max}$.

If we assume 10% (corresponding to $\delta_{\rm iso}^{\rm max} \sim 0.1$) as the maximum acceptable loss in the CMB signal due to imperfect isolation and consider typical values for the LFI receivers ($T_{\rm ref} = 4.5$ K and $T_{\rm noise}$ ranging from 10 to 30 K), we find $\epsilon_{\rm max} = 0.05$ equivalent to −13 dB, which corresponds to the requirement for LFI receivers.

B.2. Measurement

If $\Delta V_{\rm sky}$ and $\Delta V_{\rm ref}$ are the voltage output variations induced by $\Delta T = T_2 - T_1$, then it is easy to see from Eq. (B.1) (with the approximation $(1-\epsilon) \simeq 1$) that

$$\epsilon \simeq \frac{\Delta V_{\rm ref}}{\Delta V_{\rm sky} + \Delta V_{\rm ref}} \cdot \tag{B.3}$$

If the reference load temperature is not perfectly stable but varies by an amount $\Delta T_{\rm ref}$ during the measurement, this can be corrected to first order if we know the photometric constant G_0. In this case, Eq. (B.3) becomes

$$\epsilon \simeq \frac{\Delta V_{\rm ref} - G_0 \Delta T_{\rm ref}}{\Delta V_{\rm sky} + \Delta V_{\rm ref} - G_0 \Delta T_{\rm ref}} \cdot \tag{B.4}$$

Measuring the isolation accurately, however, is generally difficult and requires a very stable environment. Any change in $\Delta V_{\rm ref}$ caused by other systematic fluctuations (e.g., temperature fluctuations, $1/f$ noise fluctuations) will affect the isolation measurement causing an over- or under-estimation depending on the sign of the effect.

To estimate the accuracy in our isolation measurements, we first calculated the uncertainty caused by a systematic error in the reference load voltage output, $\Delta V_{\rm ref}^{\rm sys}$. If we substitute in Eq. (B.4) $\Delta V_{\rm ref}$ with $\Delta V_{\rm ref} \pm \Delta V_{\rm ref}^{\rm sys}$ and develop an expression to first order in $\Delta V_{\rm ref}^{\rm sys}$, we obtain

$$\epsilon \sim \epsilon_0 \mp \frac{\Delta V_{\rm sky}}{\Delta V_{\rm sky} + \Delta V_{\rm ref} - G_0 \Delta T_{\rm ref}} \Delta V_{\rm ref}^{\rm sys} \equiv \epsilon_0 \mp \delta\epsilon, \tag{B.5}$$

where we indicate by ϵ_0 the isolation given by Eq. (B.4).

We estimated $\delta\epsilon$ in our measurement conditions. Because the three temperature steps were implemented in about one day, we evaluated the total power signal stability on this timescale from a long-duration acquisition in which the instrument was left running undisturbed for about two days. For each detector datastream, we first removed spurious thermal fluctuations by performing a correlation analysis with temperature sensor data then we calculated the peak-to-peak variation in the reference load datastream.

Appendix C: Calculation of noise effective bandwidth

The well-known radiometer equation applied to the output of a single diode in the *Planck*-LFI receivers links the white noise sensitivity to sky and noise temperatures and the receiver bandwidth. It reads (Seiffert et al. 2002)

$$\delta T_{\rm rms} = 2\frac{T_{\rm sky} + T_{\rm noise}}{\sqrt{\beta}} \cdot \tag{C.1}$$

In the case of a linear response, i.e., if $V_{\rm out} = G \times (T_{\rm sky} + T_{\rm noise})$ (where G represents the photometric calibration constant) we can write Eq. (C.1) in its most useful uncalibrated form

$$\delta V_{\rm rms} = 2\frac{V_{\rm out}}{\sqrt{\beta}}, \tag{C.2}$$

which is commonly used to estimate the receiver bandwidth, β, from a simple measurement of the receiver DC output and white noise level, i.e.,

$$\tilde{\beta} = 4\left(\frac{V_{\rm out}}{\delta V_{\rm rms}}\right)^2 \cdot \tag{C.3}$$

If the response is linear and the noise is purely radiometric (i.e., all the additive noise from back-end electronics is negligible and there are no non-thermal noise inputs from the source), then $\tilde{\beta}$ is equivalent to the receiver bandwidth, i.e.,

$$\tilde{\beta} \equiv \beta = 4\left(\frac{T_{\rm sky} + T_{\rm noise}}{\delta T_{\rm rms}}\right)^2 \cdot \tag{C.4}$$

In contrast, if the receiver output is compressed, from Eq. (2) we have that

$$\delta V_{\rm rms} = \frac{\partial V_{\rm out}}{\partial T_{\rm in}} \delta T_{\rm rms}. \tag{C.5}$$

By combining Eqs. (2), (C.3) and (C.5) we find that

$$\begin{aligned}\tilde{\beta} &= 4\left(\frac{T_{\rm sky} + T_{\rm noise}}{\delta T_{\rm rms}}\right)^2 \left[1 + b\, G_0 (T_{\rm sky} + T_{\rm noise})\right]^2 \\ &\equiv \beta \left[1 + b\, G_0 (T_{\rm sky} + T_{\rm noise})\right]^2,\end{aligned} \tag{C.6}$$

which shows that $\tilde{\beta}$ is an overestimate of the "optical" bandwidth unless the non-linearity parameter b is very small.

Appendix D: White noise sensitivity calibration and extrapolation to flight conditions

We now detail the calculation needed to convert the uncalibrated white noise sensitivity measured on the ground to the expected calibrated sensitivity for in-flight conditions. The calculation starts from the general radiometric output model in Eq. (2), which can be written in the following form

$$T_{\rm out}(V_{\rm in}) = T_{\rm noise} - \frac{V_{\rm in}}{G_0(b\, V_{\rm in} - 1)} \cdot \tag{D.1}$$

Our starting point is the raw datum, which is a couple of uncalibrated white noise levels for the two detectors in a radiometer measured with the sky load at a temperature $T_{\rm sky-load}$ and the front-end unit at physical temperature $T_{\rm test}$.

From the measured uncalibrated white noise level in Volt $\rm s^{1/2}$, we attempt to derive a calibrated white noise level extrapolated to input temperature equal to $T_{\rm sky}$ and with the front.end unit at a temperature of $T_{\rm nom}$. This is achieved in three steps:

1. extrapolation to nominal front-end unit temperature;
2. extrapolation to nominal input sky temperature;
3. calibration in units of K $\rm s^{1/2}$.

In the following sections, we describe in detail the calculations underlying each step.

D.1. Step 1-extrapolate uncalibrated noise to nominal front end unit temperature

This is a non-trivial step to be performed if we wich to consider all the elements in the extrapolation. Here we focus on a zero-order approximation based on the following assumptions:

1. the radiometer noise temperature is dominated by the front-end noise temperature, such that $T_{\rm noise} \sim T^{\rm FE}_{\rm noise}$;
2. we neglect any effect on the noise temperature given by resistive losses of the front-end passive components;
3. we assume the variation in $T^{\rm FE}_{\rm noise}$ to be linear in $T_{\rm phys}$.

Based on these assumptions, the receiver noise temperature at nominal front-end temperature can be written as

$$T_{\rm noise}(T_{\rm nom}) = T_{\rm noise}(T_{\rm test}) + \frac{\partial T^{\rm FE}_{\rm noise}}{\partial T_{\rm phys}} \Delta T_{\rm phys}, \tag{D.2}$$

where $\Delta T_{\rm phys} = T_{\rm nom} - T_{\rm test}$. A similar but slightly different relationship can be derived for the gain factor G_0. We consider that $G_0 = {\rm const} \times G^{\rm FE} G^{\rm BE}$, and that we can write $G^{\rm FE}(T_{\rm nom}) = G^{\rm FE}(T_{\rm test})(1+\delta)$, where $\delta = \frac{1}{G^{\rm FE}(T_{\rm test})} \frac{\partial G^{\rm FE}}{\partial T_{\rm phys}} \Delta T_{\rm phys} = \frac{\ln(10)}{10} \frac{\partial G^{\rm FE}({\rm dB})}{\partial T_{\rm phys}} \Delta T_{\rm phys}$, i.e.,

$$G_0(T_{\rm nom}) = G_0(T_{\rm test})(1+\delta). \tag{D.3}$$

From the radiometer equation we have that $\sigma \propto (T_{\rm in} + T_{\rm noise})$, from which we can write

$$\sigma(T_{\rm nom}) \equiv \sigma^{\rm nom} = \sigma(T_{\rm test}) \frac{(T_{\rm in} + T_{\rm noise}(T_{\rm nominal}))}{(T_{\rm in} + T_{\rm noise}(T_{\rm test}))} = \\ = \sigma(T_{\rm test})(1+\eta), \tag{D.4}$$

where

$$\eta = \frac{\partial T^{\rm FE}_{\rm noise}}{\partial T_{\rm phys}} \left[(T_{\rm in} + T_{\rm noise}(T_{\rm test}))\right]^{-1} \Delta T_{\rm phys}. \tag{D.5}$$

D.2. Step 2 – extrapolate uncalibrated noise to $T_{\rm sky}$

From this point, we consider quantities such as $T_{\rm noise}$, white noise level, and G_0, extrapolated to the nominal front-end temperature using Eqs. (D.2), (D.3), and (D.4). Therefore, we now omit the superscript "nom" so that, for example, $\sigma \equiv \sigma^{\rm nom}$.

We now start from the radiometer equation in which, for each detector, the white noise spectral density is given by

$$\delta T_{\rm rms} = 2 \frac{T_{\rm in} + T_{\rm noise}}{\sqrt{\beta}} \,. \tag{D.6}$$

We now attempt to find a similar relationship for the uncalibrated white noise spectral density linking $\delta V_{\rm rms}$ to $V_{\rm out}$. We begin from Eq. (C.5) and calculate the derivative of $V_{\rm out}$ using Eq. (2) and $\delta T_{\rm rms}$ from Eq. (D.6). We obtain

$$\sigma = \frac{V_{\rm out}}{\sqrt{\beta}} \left[1 + b\, G_0 \left(T_{\rm in} + T_{\rm noise}\right)\right]^{-1} , \tag{D.7}$$

where β is the bandwidth and $V_{\rm out}$ is the DC voltage output of the receiver. Considering the two input temperatures $T_{\rm in}$ and $T_{\rm sky}$, then the ratio is

$$\frac{\sigma(T_{\rm sky})}{\sigma(T_{\rm in})} = \frac{V_{\rm out}(T_{\rm sky})}{V_{\rm out}(T_{\rm in})} \times \frac{1 + b\, G_0(T_{\rm in} + T_{\rm noise})}{1 + b\, G_0(T_{\rm sky} + T_{\rm noise})} \,. \tag{D.8}$$

If we refer to ρ as the ratio $\frac{\sigma(T_{\rm sky})}{\sigma(T_{\rm in})}$ and use Eq. (2) to place in explicit form the ratio of output voltages in Eq. (D.8) so that $\sigma(T_{\rm sky}) = \rho \times \sigma(T_{\rm in})$, we have

$$\rho = \frac{T_{\rm sky} + T_{\rm noise}}{T_{\rm in} + T_{\rm noise}} \times \left[\frac{1 + b\, G_0(T_{\rm in} + T_{\rm noise})}{1 + b\, G_0(T_{\rm sky} + T_{\rm noise})}\right]^2 . \tag{D.9}$$

D.3. Step 4-calibrate extrapolated noise

From Eqs. (D.7) and (2), we obtain

$$\sigma = \frac{G_0}{\left[1 + b\, G_0(T_{\rm sky} + T_{\rm noise})\right]^2} \times 2 \frac{T_{\rm sky} + T_{\rm noise}}{\sqrt{\beta}} \,. \tag{D.10}$$

If we call $\sigma^{\rm cal}$ the calibrated noise extrapolated at the sky temperature and consider that, by definition, $\sigma^{\rm cal} = 2\frac{T_{\rm sky}+T_{\rm noise}}{\sqrt{\beta}}$, the previous equation infers that

$$\sigma^{\rm cal} = \frac{\left[1 + b\, G_0(T_{\rm sky} + T_{\rm noise})\right]^2}{G_0} \sigma. \tag{D.11}$$

Appendix E: Weighted noise averaging

According to the LFI receiver design, the output from each radiometer is produced by combinating signals from two corresponding detector diodes. We consider two differenced and calibrated datastreams coming from two detectors of a radiometer leg, $d_1(t)$ and $d_2(t)$. The simplest way to combine the two outputs is to take a straight average, i.e.,

$$\mathrm{d}(t) = \frac{d_1(t) + d_2(t)}{2}, \tag{E.1}$$

so that the white noise level of the differenced datastream is given by $\sigma_{d(t)} = \sqrt{\sigma^2_{d_1(t)} + \sigma^2_{d_2(t)}}$. This approach, however, is not optimal in cases where the two noise levels are unbalanced, so that the noise of the averaged datastream is dominated by the noisier channel.

An alternative to Eq. (E.1) is given by a weighted average in which weights are represented by the inverse of the noise levels of the two diode datasteams, i.e.,

$$d(t) = \frac{w_1 d_1(t) + w_2 d_2(t)}{w_1 + w_2}, \tag{E.2}$$

or, more generally, in the case where we average more than two datastreams,

$$\mathrm{d}(t) = \frac{\sum_{j=1}^{N} w_j d_j(t)}{\sum_{j=1}^{N} w_j} \,. \tag{E.3}$$

For noise-weighted averaging, we choose the weights $w_j = \sigma^{-2}_{d_j(t)}$, so that the white noise of the differenced datastream is given by

$$\sigma_{d(t)} = \left(\sum_{j=1}^{N} \sigma^{-2}_{d_j(t)}\right)^{-1/2} \,. \tag{E.4}$$

Table G.1. Temperature susceptibility parameters.

	$\partial G/\partial T_{\rm phys}$(dB/K)			
	M-00	M-01	S-10	S-11
LFI18	–0.05	–0.05	–0.05	–0.05
LFI19	–0.05	–0.04	–0.02	–0.03
LFI20	–0.05	–0.04	–0.03	–0.04
LFI21	–0.07	–0.07	–0.07	–0.20
LFI22	–0.21	–0.15	–0.18	–0.13
LFI23	–0.03	–0.05	–0.05	–0.05
LFI24	–0.08	–0.06	–0.08	–0.08
LFI25	–0.02	–0.02	–0.04	–0.05
LFI26	–0.01	–0.03	–0.01	–0.01
LFI27	–0.06	–0.05	–0.04	–0.01
LFI28	–0.03	–0.07	–0.14	–0.13

	$\partial T_{\rm noise}/\partial T_{\rm phys}$(K/K)			
	M-00	M-01	S-10	S-11
LFI18	0.47	0.49	0.38	0.42
LFI19	0.36	0.33	0.40	0.37
LFI20	0.25	0.23	0.30	0.25
LFI21	0.15	0.15	0.18	0.30
LFI22	0.10	0.10	0.10	0.10
LFI23	0.10	0.16	0.17	0.16
LFI24	0.40	0.41	0.10	0.43
LFI25	0.12	0.10	0.25	0.08
LFI26	0.70	0.70	0.47	0.50
LFI27	0.81	0.45	0.58	0.34
LFI28	0.15	0.15	0.10	0.33

Notes. Gain and noise temperature susceptibilities to front-end temperature fluctuations were measured during the RCA calibration campaign.

Appendix F: Thermal susceptibility scientific requirement

Temperature fluctuations in the LFI focal plane arise primarily from variations in the sorption cooler system driven by the cycles of the six cooler compressors that "pump"[7] the hydrogen in the high-pressure piping line towards the cooler cold-end. These fluctuations exhibit a frequency spectrum dominated by a period of ∼1 h, corresponding to the global warm-up/cool-down cycle of the six compressors.

An active PID temperature stabilisation assembly at the interface between the cooler cold-end and the focal plane, achieves stabilities of the order of 80−100 mK peak-to-peak with a frequency spectrum dominated by the single compressor frequency (∼1 mHz) and the frequency of the whole assembly (∼0.2 mHz).

These fluctuations propagate through the focal plane mechanical structure, so that the true temperature instabilities at the level of the feed-amplifier systems (the term $\Delta T_{\rm phys}$ in Eq. (6)) are significantly damped. The LFI thermal model (Tomasi et al. 2010) shows that the fluctuations in the front-end modules are of the level of $\lesssim$10 mK and dominated by the "slowest" components (i.e., those with frequencies $\lesssim 10^{-2}$ Hz).

If we take into account that slow fluctuations in the antenna temperature time stream are damped further by a factor $\sim 10^3$ by the scanning strategy and map-making (Mennella et al. 2002), we can easily see from Eq. (6) that a receiver susceptibility $f_{\rm trans} \lesssim 0.1$ is required to maintain the final peak-to-peak error per pixel $\lesssim 1\ \mu$K.

Appendix G: Front-end temperature susceptibility parameters

Temperature susceptibility parameters are summarised in Table G.1.

References

Bersanelli, M., Cappellini, B., Butler, R. C., et al. 2010, A&A, 520, A4
Bhandari, P., Prina, M., Bowman, R. C., et al. 2004, Cryogenics, 44, 395
Cuttaia, F., Menella, A., Stringhetti, L., et al. 2009, JINST, 4, T12013
Davis, R., Wilkinson, A., Davies, R., et al. 2009, JINST, 4, T12002
Daywitt, W. 1989, Radiometer equation and analysis of systematic errors for the NIST automated radiometers, Tech. Rep. NIST/TN-1327, NIST
Dupac, X., & Tauber, J. 2005, A&A, 430, 363
Mandolesi, N., Bersanelli, M.., Butler, R. C., et al. 2010, A&A, 520, A3
Maris, M., Maino, D., Burigana, C., et al. 2004, A&A, 414, 777
Martin, P., Riti, J.-B., & de Chambure, D. 2004, in 5th International Conference on Space Optics, ed. B. Warmbein, ESA SP, 554, 323
Meinhold, P., Leonardi, R., Aja, B., et al. 2009, JINST, 4, T12009
Mennella, A., Bersanelli, M., Burigana, C., et al. 2002, A&A, 384, 736
Mennella, A., Bersanelli, M., Seiffert, M., et al. 2003, A&A, 410, 1089
Mennella, A., Villa, F., Terenzi, L., et al. 2009, JINST, 4, T12011
Seiffert, M., Mennella, A., Burigana, C., et al. 2002, A&A, 391, 1185
Tauber, J. A., Norgaard-Nielsen, H. U., Ade, P. A. R., et al. 2010, A&A, 520, A2
Terenzi, L., Lapolla, M., Laaninen, M., et al. 2009a, JINST, 4, T12015
Terenzi, L., Salmon, M., Colin, A., et al. 2009b, JINST, 4, T12012
Tomasi, M., Cappellini, B., Gregorio, A., et al. 2010, JINST, 5, T01002
Valenziano, L., Cuttaia, F., De Rosa, A., et al. 2009, JINST, 4, T12006
Varis, J., Hughes, N., Laaninen, M., et al. 2009, JINST, 4, T12001
Villa, F., Bersanelli, M., Burigana, C., et al. 2002, in Experimental Cosmology at Millimetre Wavelengths, ed. M. de Petris, & M. Gervasi, AIP Conf. Ser., 616, 224
Villa, F., Terenzi, L., Sandri, M., et al. 2010, A&A, 520, A6
Wade, L., Bhandari, P., Bowman, J. R., et al. 2000, in Advances in Cryogenic Engineering, 45A, ed. Q.-S. Shu et al. (Kluwer Academic/Plenum New York), 499
Zonca, A., Franceschet, C., Battaglia, P., et al. 2009, JINST, 4, T12010

[7] The sorption cooler does not use mechanical compressors to generate a high pressure flow, but a process of absorption-desorption of hydrogen into six hydride beds, the "compressors" being controlled by a temperature modulation of the beds themselves.